Optical and Quantum Communications

Academic and Research Staff
Professor Jeffrey H. Shapiro, Dr. Franco N. C. Wong, Dr. Vittorio Giovannetti, Dr. Lorenzo Maccone, Dr. Gaetan Messin

Graduate Students
Marius A. Albota, Joe Aung, Baris I. Erkmen, Shane M. Haas, Eser Keskiner, Christopher E. Kuklewicz, Elliott J. Mason, Emily W. Nelson, Mohsen Razavi, Brent J. Yen

Undergraduate Student
Corey Scott

The central theme of our programs has been to advance the understanding of optical and quantum communication, radar, and sensing systems. Broadly speaking, this has entailed: (1) developing system-analytic models for important propagation, detection, and communication scenarios; (2) using these models to derive the fundamental limits on system performance; and (3) identifying, and establishing through experimentation the feasibility of, techniques and devices which can be used to approach these performance limits.

1. Quantum Information and Communication

Sponsors
Army Research Office - Grant DAAD-19-00-1-0177
MIT Lincoln Laboratory - Contract BX-7466
National Reconnaissance Office - Contract NRO-000-00-C-0032
National Reconnaissance Office - Contract NRO-000-00-C-0158
Army Research Office - Grant DAAD-19-01-1-0647
Air Force Research Laboratory - Cooperative Agreement F30602-01-2-0546

Project Staff
Professor Jeffrey H. Shapiro, Dr. Franco N. C. Wong, Dr. Vittorio Giovannetti, Dr. Lorenzo Maccone, Dr. Gaetan Messin, Marius A. Albota, Joe Aung, Eser Keskiner, Christopher E. Kuklewicz, Elliott J. Mason, Emily W. Nelson, Brent J. Yen

We are embarked on research in the area of quantum information technology whose goal is to enable the quantum-mechanical information transmission, storage, and processing needed for future applications in quantum computing and quantum communication. Our theoretical work in this area has focused on architectural designs for long-distance teleportation and multi-party entanglement transmission, and on novel applications of entanglement. Of particular interest has been the identification of high-performance means for generating the polarization-entangled photons needed for many quantum information applications, including teleportation, entanglement-based quantum positioning and clock synchronization, and quantum secret sharing.

Architectural Analysis The preeminent obstacle to the development of quantum information technology is the difficulty of transmitting quantum information over noisy and lossy quantum communication channels, recovering and refreshing the quantum information that is received, and then storing it in a reliable quantum memory. Together with Professor Seth Lloyd and Dr. Selim Shahriar of RLE, and Dr. Phillip Hemmer of the Air Force Research Laboratory, we have proposed and analyzed a novel architecture for the singlet-state approach to quantum teleportation [1]. A simple block diagram of this architecture is shown in Fig. 1. It consists of an ultrabright narrowband source of polarization-entangled photons pairs (*P*), connected to a pair of trapped Rb atom quantum memories (*M*) by transmission through *L*-km-long lengths of standard telecommunication fiber.

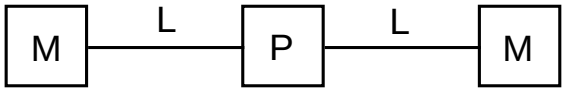

Figure 1. Schematic of long-distance quantum communication system: *P* = ultrabright narrowband source of polarization-entangled photon pairs; *L* = *L* km of standard telecommunication fiber; *M* = trapped atom quantum memory.

Each *M* block in Fig. 1 is a quantum memory in which a single ultracold ^{87}Rb atom is confined by a CO_2-laser trap in an ultra-high vacuum chamber with cryogenic walls within a high-finesse single-ended optical cavity. An abstract representation of the relevant hyperfine levels for such a memory is given in Fig. 2(a). A 795 nm photon in an arbitrary polarization can be absorbed, transferring the qubit from the photon to the degenerate *B* levels of Fig. 2(a), and thence to long-lived storage levels, by coherently driving the *B*-to-*D* transitions. By means of optically-off-resonant (OOR) transitions, the Bell states of two atoms in a single vacuum-chamber trap can be converted into superposition states of one of the atoms. All four Bell measurements needed for the Bennett *et al*. singlet-state teleportation process [2] can then be made, sequentially, by detecting the presence (or absence) of fluorescence as an appropriate sequence of OOR laser pulses is applied to the latter atom. The Bell-measurement results (two bits of classical information) in one memory can be sent to a distant memory, where (at most) two additional OOR pulses are needed to complete the state transformation process. More details on this memory, and its use in teleportation, are given in [3].

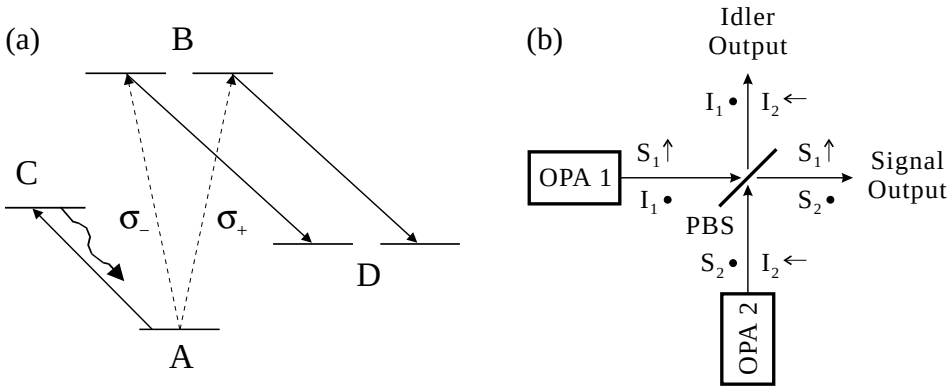

Figure 2. Essential components of singlet-state quantum communication system from Fig. 1. Left (a), simplified atomic-level schematic of the trapped Rb atom quantum memory: *A*-to-*B* transition occurs when one photon from an entangled pair is absorbed; *B*-to-*D* transition is coherently driven to enable storage in the long-lived *D* levels; *A*-to-*C* cycling transition permits nondestructive determination of when a photon has been absorbed. Right (b), ultrabright narrowband source of polarization-entangled photon pairs: each optical parametric amplifier (OPA1 and OPA2) is type-II phase matched; for each optical beam the propagation direction is *z*, and *x* and *y* polarizations are denoted by arrows and bullets, respectively; PBS, polarizing beam splitter.

The *P* block in Fig. 1 is an ultrabright narrowband source of polarization-entangled photon pairs [4], capable of producing ~10^6 pairs/sec in ~30 MHz bandwidth by appropriately combining the signal and idler output beams from two doubly-resonant type-II phase matched optical parametric amplifiers (OPAs), as sketched in Fig. 2(b). The importance of our resonant approach to entanglement generation is the need to achieve high flux within the narrow linewidth of the Rb atom memory; existing parametric downconverter sources of entanglement are far too broadband to permit useful transmission rates in the Fig. 1 architecture.

During the past year we have augmented and generalized our performance analysis for the preceding teleportation architecture in several ways. First, we have shown that a single

degenerate OPA provides a simpler, but somewhat less effective, source for long-distance teleportation in the Fig. 1 architecture [5,6]. With probability one half, this source, which is shown schematically in Fig. 3, produces a polarization triplet state at the output of the 50/50 beam splitter whenever an OPA photon pair enters that beam splitter. The Bennett *et al*. singlet-state teleportation protocol is easily modified to accommodate the triplet source; alternatively, the phase of the signal beam's *y*-polarization can be phase shifted, after the 50/50 beam splitter, to convert the triplet into a singlet.

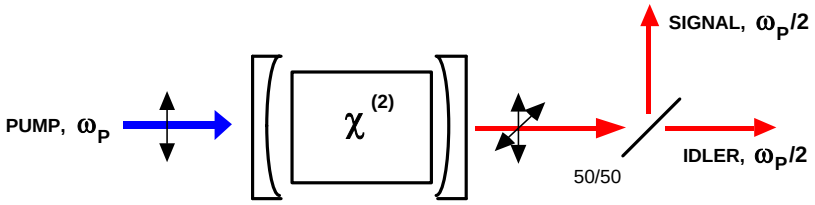

Figure 3. Doubly-resonant, type-II phase matched degenerate OPA. Signal and idler photons emerge in frequency-degenerate, orthogonally-polarized pairs from the OPA cavity. The joint state of the beams exiting the 50/50 beam splitter is mixed, but includes a triplet component that can be used as the entanglement source in the Fig. 1 teleportation architecture.

Figure 4 compares the achievable throughput and required OPA gains for gain-optimized teleportation using the dual-OPA and degenerate OPA sources. These curves presume 500 kHz memory cycling rate, 5 dB of fixed loss for each source-to-memory path, 0.2 dB/km loss in the optical fiber, and 0.5 ratio of memory-cavity linewidth to source-cavity linewidth. In both cases, the OPA gain is optimized to maximize throughput subject to the constraint that the loss-limited fidelity be 95%. The details of these calculations are given in [5]. Figure 4 shows that both the dual-OPA and the degenerate OPA are capable of sustaining substantial throughputs over distances as long as 50 km, with the former enjoying a 6 dB performance advantage over the latter. The origins of this 6 dB advantage are easily explained. Each amplifier in the dual-OPA system uses roughly the same gain as does the degenerate-OPA system, thus the dual-OPA has twice the raw flux of the degenerate OPA. Furthermore, the polarizing beam splitter in the dual-OPA source losslessly combines the outputs from the two OPAs in Fig. 2(b), whereas the degenerate OPA suffers a 50% loss when both photons from a single pair exit from the same port of the 50/50 beam splitter in Fig. 3. Note that the degenerate-OPA system cannot recoup its 6 dB performance loss merely by increasing its OPA gain because increased gain increases the likelihood that multiple pairs are generated, hence reducing the teleportation fidelity.

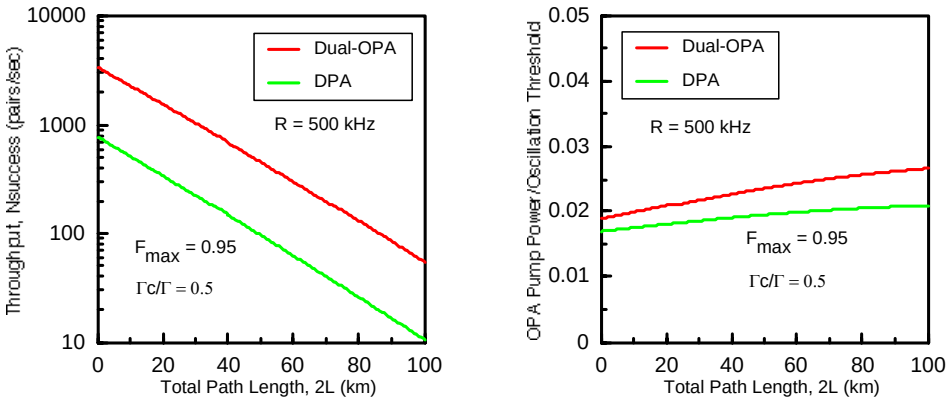

Figure 4. Gain-optimized performance of the Fig. 1 architecture for dual-OPA and degenerate parametric amplifier (DPA) source configurations. Left panel: throughput versus total path length. Right panel: normalized OPA gain versus total path length. All curves assume 5 dB of excess loss per *P*-to-*M* block connection, 0.2 dB/km fiber-propagation loss, 0.5 ratio of memory-cavity linewidth to source-cavity linewidth, and 500 kHz memory cycling rate.

Singlet-state teleportation relies on two-particle entanglement. There is considerable interest currently in *N*-party entanglement, i.e., in the generation and application of entangled states of *N*>2 particles. Greenberger, Horne, and Zeilinger showed that such multi-particle states were of fundamental importance because they led to conflicts with local realism for nonstatistical predictions of quantum mechanics [7]. The simplest state of this Greenberger-Horne-Zeilinger (GHZ) class, viz., $(|\uparrow\rangle\ |\uparrow\rangle|\bullet\rangle+|\bullet\rangle|\bullet\rangle|\uparrow\rangle)/2^{1/2}$, has been shown, theoretically, to permit quantum secret sharing [8]. The initial experimental demonstration of GHZ-state generation by Bouwmeester *et al*. [9], like their earlier work on singlet-state teleportation, was an annihilative table-top measurement. Moreover it had an extremely low flux: 1 GHZ state every 150 seconds. We have shown that our quantum teleportation architecture, diagrammed in Fig. 1, can lead to long-distance transmission and storage of GHZ states via an alerted detection scheme akin to that in [9].

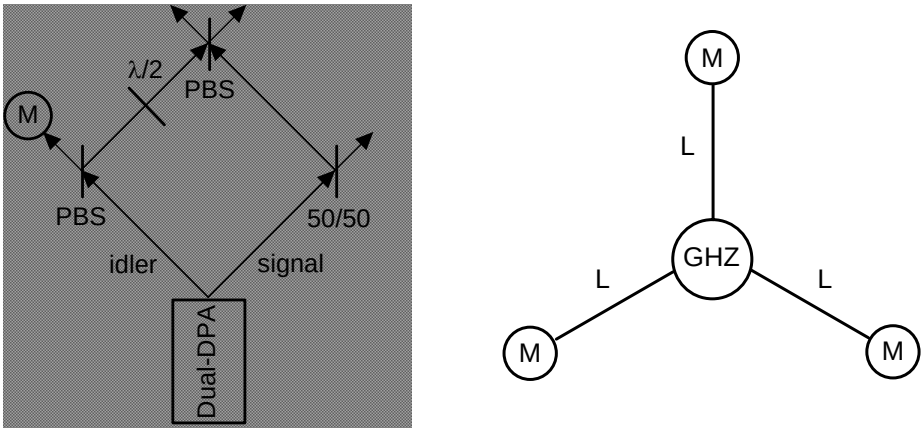

Figure 5. Left panel: degenerate parametric amplifier system for generation of GHZ states. Dual degenerate parametric amplifier (dual-DPA) is a Fig. 2(b) arrangement in which OPAs 1 and 2 operate at frequency degeneracy and are pumped in phase. PBS polarizing beam splitter; *M* trapped-Rb atom quantum memory; λ/2 half-wave plate. Right panel: Long-distance communication architecture for GHZ states. GHZ is the source arrangement from the left panel or from Fig. 7.

The system in Fig. 5 is run under a clocked protocol. In each time epoch we monitor the cycling transitions on all four quantum memories, viz., the three external memories shown in the right panel of Fig. 5, plus the fourth memory (internal to the source block in that panel) that is present in the left panel of Fig. 5. The loading protocol is repeated until all four memories absorb photons in the same time epoch. As shown for annihilative measurements in [9], when all four memories in Fig. 5 have absorbed photons, and these photons came from the emission of two entangled signal-idler pairs from the dual-DPA, then the three external memories have been loaded into a GHZ state.

We have carried out a loss-limited performance analysis [5] of this GHZ-state communication scheme; its results are shown in Fig. 6. The left panel in this figure shows the maximum throughput that can be achieved when the conditional probability of loading a GHZ state, given that there has not been an erasure, is 0.9. The right panel shows the DPA gain value needed to achieve these throughput results. The greatly reduced likelihood that a dual-DPA produces two signal-idler pairs in a loading interval — as compared to its probability of producing one such pair — is the primary reason that the GHZ-state throughput in Fig. 6 is so much lower than the teleportation throughput we saw in Fig. 4. On the positive side, however, we see that the architecture from Fig. 5 permits a throughput comparable to what Bouwmeester *et al*. produced in the laboratory to be realized over a 10 km source-to-memory radius with 90% conditional probability of success. More important, though, is the fact that the memories in the Fig. 5 architecture allow the GHZ state to be stored for use in quantum secret sharing or other applications of 3-particle entanglement.

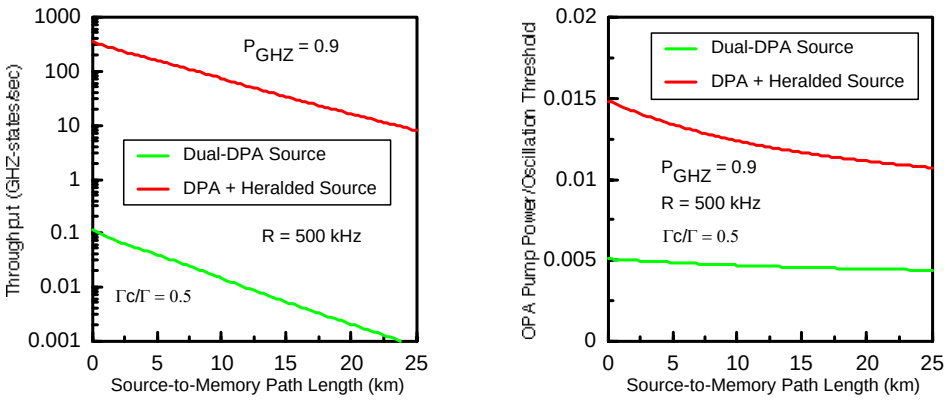

Figure 6. Gain-optimized performance for the Fig. 5 architecture. Left panel: GHZ-state throughput versus source-to-memory path length for dual degenerate parametric amplifier (dual-DPA) and DPA plus heralded single-photon sources. Right panel: normalized DPA gain versus source-to-memory path length. All curves assume 5 dB of excess loss per source-to-memory connection, 0.2 dB/km fiber-propagation loss, 0.5 ratio of memory-cavity linewidth to source-cavity linewidth, and 500 kHz memory cycling rate.

A route to obtaining substantially higher throughputs from the Fig. 5 architecture may be developed by examining the role of the memory element in the left panel of that figure. Suppose that the dual-DPA emits two entangled-photon pairs from which each of the memories in Fig. 5 captures one photon. The polarization of the photon captured by the memory in the left panel of Fig. 5 is determined, by the polarizing beam splitter, as is the polarization of the photon entering the half-wave plate in that panel. The half-wave plate's orientation forces the latter photon to have a 50/50 chance of taking either output port of the ensuing polarizing beam splitter. It then follows that the three external memories share a GHZ state. Note that the sole purpose of the memory that is internal to the source is to serve as a trigger, i.e., to herald (by its absorbing a photon of a definite polarization) the presence of a photon in the orthogonal polarization at the input to the half-wave plate. Recent work has shown that it may be possible to construct heralded single-photon sources [10]. With such a source, used in the configuration shown in Fig. 7, there would be a single photon entering the half-wave plate during every cycle of the loading protocol, as compared to the much lower flux that prevails when the source from the left panel of Fig. 5 is used. When this heralded source produces one photon per loading interval in the proper spatio-temporal mode for coupling to the trapped-atom quantum memory, vastly improved GHZ-state communication results from using the Fig. 7 source in the transmission architecture shown in the right panel of Fig. 5. As shown in Fig. 6, throughput rises by more than three orders of magnitude, to more than 70 GHZ states/sec at 10 km radius. Note that the source-to-memory radius for which GHZ-state communication can be achieved may be extended by teleporting the contents of any or all of GHZ-state containing memories from Fig. 5 using the long-distance teleportation architecture shown in Fig. 1. Thus, it should be possible to share GHZ states over long distances for use in quantum secret sharing or other multi-party entanglement protocols.

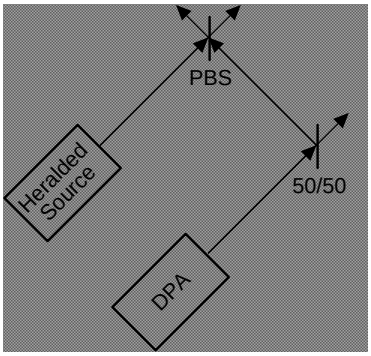

Figure 7. Heralded single-photon source plus degenerate parametric amplifier for GHZ-state generation.

In our continuing work on architectural analysis we are developing a more complete quantum communication model for the telportation architecture, from which the performance improvements afforded by the use of quantum error-correcting codes and/or entanglement purification protocols may be assessed.

Entanglement Applications In addition to our fundamental architectural studies of quantum teleportation and multi-party entanglement transmission, we have made a number of theoretical advances concerning the applications of entanglement. Prior work by Professor Seth Lloyd and members of our group [11] has shown that entanglement can be used to substantially improve the performance of positioning and ranging systems. The *N*-mode entangled state that is needed to realize these performance gains is of the form,

$$|\psi\rangle = \int \frac{d\omega}{2\pi}\phi(\omega)|\omega\rangle_1|\omega\rangle_2\cdots|\omega\rangle_N,$$

i.e., it comprises a superposition — with spectral function $\phi(\omega)$ — of *N* modes, each containing a single photon of the same frequency, ω. Using this state, the mean-squared error in time-of-flight measurements can be reduced by a factor of *N*. Realizing this advantage, however, will require new approaches to the generation of entangled photon states.

The usual, parametric downconverter technique is essentially limited to the *N*=2 (bi-photon) case. Furthermore, at frequency degeneracy and with the usual phase-matching conditions, parametric downconversion produces the twin-beam (TB) bi-photon state,

$$|TB\rangle = \int \frac{d\omega}{2\pi}\phi(\omega)\left|\frac{\omega_p}{2}+\omega\right\rangle_S\left|\frac{\omega_p}{2}-\omega\right\rangle_I,$$

for its signal (S) and idler (I) modes and pump frequency ω_p, whereas the N=2 version of the state needed for improved positioning is the difference-beam (DB) bi-photon state,

$$|DB\rangle = \int \frac{d\omega}{2\pi}\phi(\omega)\left|\frac{\omega_p}{2}+\omega\right\rangle_S\left|\frac{\omega_p}{2}+\omega\right\rangle_I.$$

We have recently shown [12] that a pulsed parametric downconverter, using a long crystal and operated in accord with novel, extended phase-matching conditions, can produce this difference-beam state. Moreover, our analysis indicates that an experimental demonstration of DB-state generation should be possible using periodically-poled potassium titanyl phosphate (PPKTP) and a pump wavelength of 790.3 nm. The distinctions between the TB and DB states can be revealed, in such a setup, by comparing the quantum interference patterns seen in Mach-Zehnder and Hong-Ou-Mandel interferometers under two alternative pumping schemes. When the PPKTP crystal is pumped by a continuous-wave source TB states are produced; and when it is pumped by a train of 167 fsec pulses a train of DB states is generated [12]. Initial plans for performing these quantum interference experiments are now being made. Theoretical work is continuing on the physics of the DB-state source.

Another area of application interest for entangled states is clock synchronization. Work done by Professor Seth Lloyd and members of our group has led to a new *classical* protocol for clock synchronization [13]: conveyor-belt synchronization. This scheme is shown schematically in Fig. 8. An inelastic conveyor belt moves from “Alice” (station *A*) to “Bob” (station *B*) and then back to “Alice” (station *A*’) at a known constant speed. This conveyor belt is capable of carrying what we shall call “sand.” Alice and Bob are able to add and/or remove sand from the conveyor belt as it passes their location, as well as measure the amount of sand that passes them on the belt. The protocol for synchronizing a pair of highly-stable clocks held by Alice and Bob, respectively, is as

follows. Starting at her clock's time zero (denoted 0_A), Alice adds sand to the belt at point *A* at a rate that is *k* times the current reading on her clock. Starting at his clock's time zero (denoted 0_B), Bob removes an amount of sand from the belt at point *B* at a rate that is 2*k* times the current reading on his clock. Alice then adds sand to the belt at point A' at a rate that is *k* times the current reading on her clock. After steady state has been reached, the amount of sand that Alice sees on the belt at the measurement point M is linearly related to the time difference 0_A-0_B.

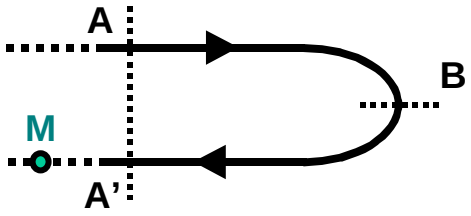

Figure 8. Schematic of classical, conveyor-belt clock synchronization.

The Fig. 8 approach to clock synchronization might be realized with light pulses instead of "sand," e.g., by modulating the phase of the pulses passing points *A*, *B*, and *A*'. However dispersive effects within the propagation medium between Alice and Bob seriously undercut the effectiveness of such a direct implementation. It is known, however, that dispersive effects cancel out in quantum interference measurements made on a bi-photon state using a Hong-Ou-Mandel interferometer [14]. We have shown [15] how this bi-photon dispersion cancellation can be combined with the classical concept of conveyor-belt clock synchronization. The basic idea is shown in Fig. 9. Photon pairs, from the signal and idler of a parametric downconverter, propagating from Alice to Bob and back are the conveyor belt. The amounts of "sand" that are added/subtracted as required by the classical protocol are the time shifts imposed within the boxes labeled *A*, *B*, and *A*' in Fig. 9. The measurement that provides the synchronization information is the time location of the coincidence-counting dip in the Hong-Ou-Mandel interferometer, shown by the beam splitter (BS) and photon coincidence (PC) blocks in Fig. 9.

Preliminary planning is underway for demonstrating the optical version of classical conveyor-belt clock synchronization, which will not enjoy dispersion cancellation, as well as a downconverter quantum version in which dispersion cancellation will occur. Other theoretical work, in the area of entanglement sources, is focusing on the novel quantum interference effects that arise in appropriately configured optical parametric amplifiers, such as the OPAs proposed for the quantum teleportation architecture. Possible applications of these new entanglement manifestations will be sought.

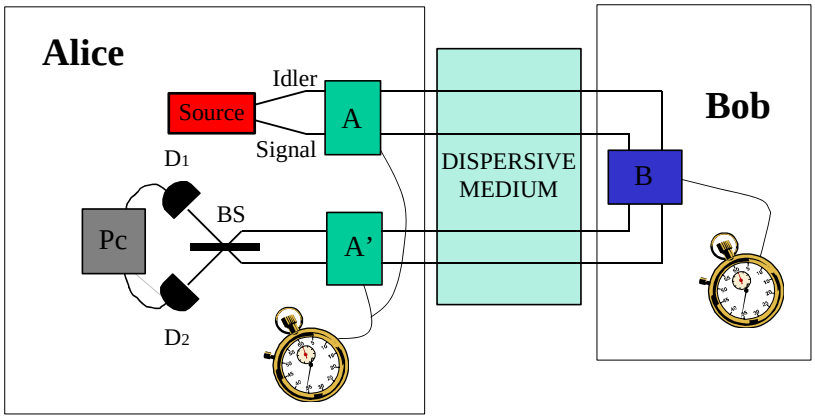

Figure 9. Schematic of quantum conveyor-belt clock synchronization, in which dispersive effects in the propagation medium cancel out in the Hong-Ou-Mandel interferometer timing measurement.

Doubly Resonant Optical Parametric Amplifier Entanglement Source We have implemented the degenerate OPA source of Fig. 3 in a 532-nm-pumped type-II phase-matched, doubly-resonant potassium titanyl phosphate (KTP) OPA [6]. In comparison to the usual spontaneous parametric downconversion, the doubly-resonant amplifier (DRA) has a substantially lower pump-power requirement, dramatically narrower output bandwidths and well-defined spatial modes, which would allow optimal coupling into trapped-atom cavities in the singlet-based teleportation architecture.

The signal and idler outputs from a DRA are composed of three components. When tuned appropriately, there will be one narrowband doubly-resonant mode pair from the DRA. In addition, however, there are narrowband singly-resonant mode pairs, for which either the signal or idler field is resonant with the cavity. There are also broadband nonresonant mode pairs, for which neither of the output fields is resonant with the cavity. The generation rate for the doubly-resonant mode pair is given by [4],

$$R_2 = G^2\Gamma,$$

where G^2 is the pump power level normalized to the pump threshold power, typically of the order of 0.01 for quantum communication applications, and Γ/π is the cavity bandwidth, of the order of tens of MHz.

The singly-resonant pair production rate R_1 can be expressed in terms of R_2,

$$R_1 = 2R_2\left(\frac{(T+L)^2}{4T}\right)\left(\frac{B_{SRO}}{B_{DRO}}\right)\left(\frac{B_{PM}}{FSR}\right),$$

where T is the output coupler transmission, L is the cavity's roundtrip excess loss, $B_{SRO} = \Gamma/\pi$ is the bandwidth of a singly-resonant oscillator (SRO) cavity, $B_{DRO} = (\sqrt{2} - 1)^{1/2}\, B_{SRO}$ is the bandwidth of a doubly-resonant oscillator (DRO) cavity, B_{PM} is the phase-matching bandwidth of the crystal, and FSR is the average free spectral range of the cavity. Relative to the doubly-resonant pair output, the effective threshold power in singly-resonant pair generation is raised, because the enhancement due to the second resonance is no longer available. This decreased pumping level leads to the first factor in parentheses on the right in the R_1 equation. The second term in parentheses is the ratio of the effective cavity bandwidths for the singly-resonant and doubly-resonant modes. Typically, by design, there is only one doubly-resonant mode pair in type-II phase matching, but singly-resonant mode pairs occur every free spectral range FSR. This leads to the final factor in parentheses, which accounts for the number of such mode spacings that occur within the crystal's phase-matching bandwidth B_{PM}. The factor of two on the right in the R_1 generation rate arises from there being two sets of singly-resonant modes pairs, one when the signal is resonant and one when the idler is resonant.

The flux of the broadband nonresonant mode pairs also satisfies a simple scaling relation with respect to the doubly-resonant flux:

$$R_0 = R_2\left(\frac{(T+L)^2}{4T}\right)^2\left(\frac{B_{PM}}{B_{DRO}}\right).$$

Here, the cavity-enhancement factor is squared because there is no resonance for either field, and the bandwidth factor represents the output's coming from the entire phase-matching bandwidth rather than just the doubly-resonant bandwidth. For our DRA system, we have T = 2.7%, L = 0.56%, B_{SRO} = 30 MHz, B_{DRO} = 20 MHz, B_{PM} = 320 GHz, and FSR = 5.6 GHz. Thus, we expect that our DRA system would have 36% of its output flux coming from nonresonant

mode pairs, 41% coming from singly-resonant mode pairs, and the remaining 23% coming from doubly-resonant mode pairs.

Figure 10 shows a measurement of the singles counts as the cavity length was scanned with the DRA operating near frequency degeneracy. These data were taken with 3 mW of pump power and detected using a Si single-photon counter with an overall quantum efficiency of ~1%, with each data point representing 10 ms of counts. The periodic behavior in Fig. 10 occurring with a 266-nm peak-to-peak spacing is due to there being a very weak residual cavity resonance at the 532-nm pump wavelength. The smaller, higher spatial-frequency modulation of the singles is due to the sequence of double resonances that were encountered as the cavity was scanned. From the minima and maxima of the counts in Fig. 10, we estimate that the ratio of the doubly-resonant counts to the total counts is ~15%, a number that is close to our $R_2 /(R_0 + R_1 + R_2)$ ~ 23% estimate, given our uncertainties in estimating the various bandwidths and the sensitivity of R_2 to cavity alignment. We also estimate from Fig. 10 a pair production rate of 1.7 x 10^7/s/mW of pump power.

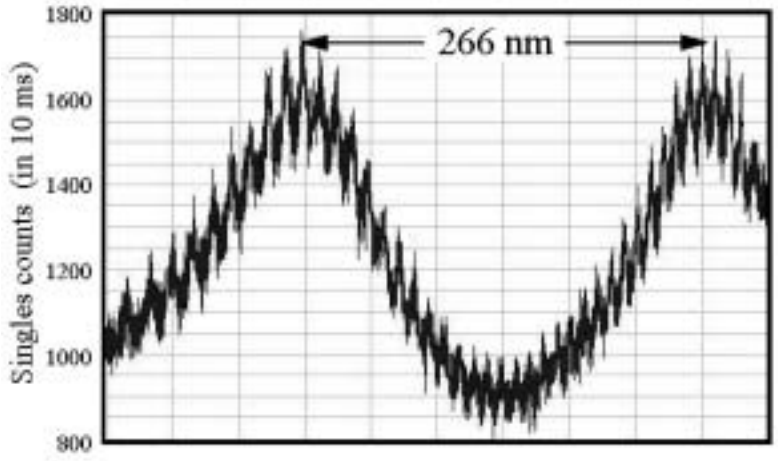

Figure 10. Singles counts of KTP DRA as a function of cavity-length tuning. Weak cavity resonance of the 532-nm pump yields the peak-to-peak cavity length change of 266 nm, and the double resonance peaks occurs at ~9.5 nm intervals.

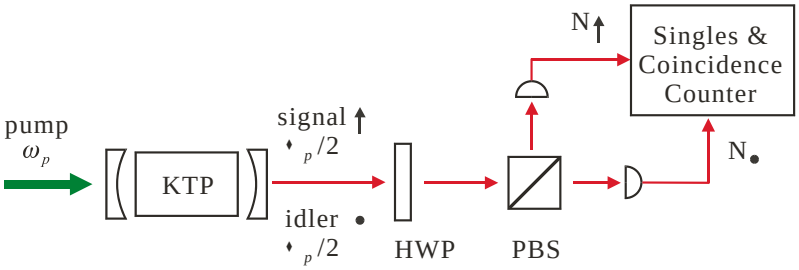

Figure 11. Schematic of a high-flux source of polarization-entangled photon pairs based on a type-II phase-matched KTP DRA.

As shown in Fig. 11, the collinearly propagating signal and idler outputs from the DRA were collimated and then passed through a half-wave plate (HWP) followed by a polarizing beam splitter (PBS) for analysis. Coincidence counting measurements were made using Si single-photon detectors located at the outputs of the PBS. The DRA output polarizations were rotated with the HWP by either $\theta = 0$ or $\theta = \pi/4$. At $\theta = 0$, the orthogonally-polarized signal and idler photons of all three output components were separated by the PBS and perfect coincidences should occur for unity quantum efficiency detection. In postdetection processing we took a $T_M = 5$

s measurement interval and, within that interval, computed C(*T*), the average number of coincidences that occurred in a duration-*T* time bin. The data in Fig. 12 were taken with a pump power of ~100 μW and the average singles counts for $\theta = 0$ were 20000 (22000 for $\theta = \pi/4$) over the 5-s measurement interval. The solid squares in Fig. 12 show C(*T*) vs. *T* with no rotation of the output polarization ($\theta = 0$). For small values of *T*, Fig. 12 shows that C(*T*) for $\theta = 0$ decreases sharply. This fall-off is because the average photon lifetime in the DRA cavity was of the order of 10 ns; the coincidence interval must be appreciably longer than the intracavity photon lifetime to have high confidence that both the signal and the idler photons have been emitted [4]. Beyond the short-*T* region, the $\theta = 0$ data points for $T > 150$ ns can be fit to a straight line whose $T = 0$ intercept is $C_{int}(0) = 44$, which gives the true value of the coincidence counts, viz., the value that prevails when *T* is much greater than the DRA's intracavity photon lifetime and accidental coincidences are eliminated.

The open squares in Fig. 12 show C(*T*) vs. *T* obtained from $T_M = 5$ s data taken with $\theta = \pi/4$. We see that the slopes of the two C(*T*) curves are essentially the same, but their $T = 0$ intercepts are different: $C_{int}(0) = 14$ for $\theta = \pi/4$, whereas $C_{int}(0) = 44$ for $\theta = 0$. Part of this reduction was due to a 50/50 beam splitter effect for frequency distinguishable photons with the rest being a consequence of quantum interference between the broadband nonresonant photon pairs, which are in a polarization-entangled triplet state. We can infer that the generation rate for the broadband polarization-entangled triplet component is 6×10^6/s/mW of pump power over a bandwidth of 320 GHz. This is a significantly higher brightness than those for previously reported sources. The improvement in production efficiency is due to the use of a highly nonlinear crystal, KTP, and collinear propagation in a long crystal. Assuming that only the nonresonant mode pairs gave perfect quantum interference, then the intercept ratio should be equal to $(R_1 + R_2)/2(R_0 + R_1 + R_2)$. This ratio can be estimated from the relative contributions of the nonresonant, singly-resonant, and doubly-resonant mode pairs (36%, 41%, and 23%, respectively), which yield 0.32, in excellent agreement with the observed value $C_{int}(\theta = \pi/4) / C_{int}(\theta = 0) = 0.32$.

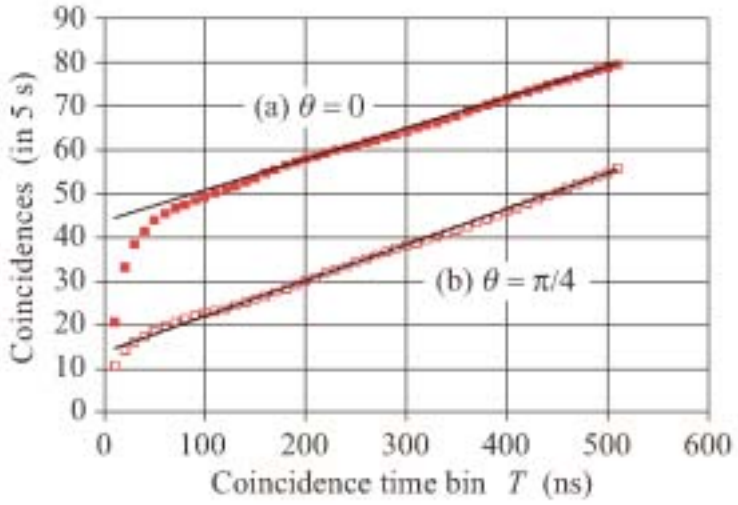

Figure 12. Coincidence counts vs. time bin *T* for $T_M = 5$ s: (a) $\theta = 0$, and (b) $\theta = \pi/4$. Straight-line fits of the $T > 150$ ns data yield coincidence intercepts of 44 for (a) and 14 for (b).

High-Flux Entanglement Sources using Periodically Poled Nonlinear Crystals We have investigated the use of periodically poled KTP (PPKTP) and lithium niobate (PPLN) as the nonlinear optical crystals for the generation of entangled photons. Quasi-phase matching in periodically poled materials allows operation at user-specified wavelengths by varying the grating periods of the nonlinear materials. For a grating period of 8.9 μm in type-II phase matched PPKTP, the downconverter was operated at frequency degeneracy at 795 nm, a wavelength that matches that of the Rb-based quantum memory in our teleportation architecture. Preliminary

measurements in a single-pass configuration of the PPKTP downconverter show that as much as 98% of the broadband (~250 GHz) collinearly-propagating photons were in a polarization-entangled triplet state. We also measured a flux of over 10^5 pairs/s for a pump power of 10 mW from a UV diode laser. We will further characterize this single-pass PPKTP downconverter for use in a singly-resonant cavity configuration to improve pair production efficiency and to obtain narrowband outputs.

We have also implemented a 532-nm-pumped PPLN downconverter that was type-I quasi-phase matched (using a third-order grating) to generate collinearly propagating outputs at ~795 nm and ~1610 nm. The system was designed to be pumped from both ends of the crystal, thus allowing downconverted outputs in the forward and backward directions to be combined at a PBS to yield frequency-nondegenerate polarization-entangled outputs. The PPLN downconverter could be temperature tuned to yield tunable outputs with a tuning range of several tens of nm. From measurements we infer a pair production rate of ~1.5 x 10^7/s/mW of pump power, similar to that of the KTP cavity system. We have made coincidence-counting measurements with a high signal-to-noise ratio and verified that the photon pairs were coincident within 6 ns. We will continue to explore this PPLN system to obtain polarization-entangled outputs.

InGaAs Single-Photon Detector In order to efficiently detect the 1610-nm output from the PPLN downconverter we have constructed an InGaAs single-photon counter based on commercially available InGaAs avalanche photodiodes (APDs). The APDs were operated in the Geiger mode by biasing the photodiodes beyond their breakdown voltage for a short duration (10-100 ns). In order to reduce the dark counts, the APDs were cooled with a 3-stage solid-state thermal-electric cooler to –50°C. With an over-bias of 2.5 V, we obtained a detection quantum efficiency of ~20% with a dark count rate of ~5.5 x 10^4/s, which is comparable to the best that has been reported. With its compact size and solid-state temperature tuning (no dry ice or liquid nitrogen), the InGaAs single-photon detector can be used at various operating points for optimal detection. One of these detectors has been used for characterizing the PPLN downconverter source.

2. Atmospheric Optical Communications

Sponsor
Defense Advanced Research Projects Agency - Grant MD1972-00-1-0012

Project Staff
Professor Jeffrey H. Shapiro, Dr. Franco N. C. Wong, Baris I. Erkmen, Shane M. Haas, Mohsen Razavi

In future battlefield operations, communications and data networking will play a much more significant role. Properly designed optical communication systems operating over atmospheric paths may be able to provide covert, high burst rate communications with the necessary quick set up and tear down capability. Laser beams propagating through the atmosphere are subject to a wide variety of deleterious effects, including absorption, depolarization, beam spread, angular spread, multipath spread, Doppler spread, and fading. These effects, which represent the combined impact of the atmosphere's molecular constituents, entrained aerosols and hydrometeors, and turbulence-induced refractive index fluctuations, may drastically curtail the performance of an atmospheric optical link. We are working, in collaboration with Professor Vincent Chan of the Laboratory for Information and Decision Systems, to: provide understanding of battlefield optical communication applications and their implied demands on optical systems; develop architectural constructs that are attainable, but make maximum use of device and subsystem capability to achieve high overall performance; and develop and demonstrate key system concepts in an experimental test bed facility.

The central focus of this program is to address the effects of atmospheric turbulence and how it may be mitigated through the use of diversity techniques in space, time, and frequency. Our

work in this regard includes both theoretical and experimental efforts. Our initial theoretical work addressed the use of space-time coding (STC) for turbulence mitigation. An STC system uses multiple transmit and receive antennas, as shown in Fig. 13, to combine temporal and spatial diversity. Tarokh *et al*. [16] have established design criteria of space-time codes for wireless communications at microwave frequencies, for which the channel is modeled by Rayleigh or Ricean fading with additive white Gaussian noise. Optical receivers that employ heterodyne detection are subject to additive white Gaussian noise, but optical propagation through atmospheric turbulence suffers from lognormal fading, not Rayleigh or Ricean fading [17]. We have shown [18] that a subset of the Tarokh *et al*. space-time codes — the orthogonal designs — minimizes the pairwise error probability for the lognormal channel. Our approach, which relies on a Central Limit Theorem approximation, extends to other fading channels with zero-mean, statistically independent path gains. Moreover, we have evaluated the exact pairwise error probability for the case of orthogonal designs, and shown that the Central Limit Theorem approximation is accurate in the performance regime of interest, see Fig. 14.

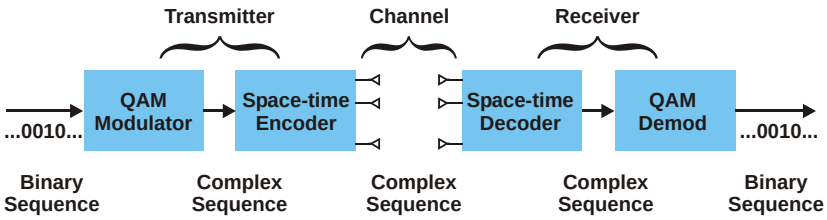

Figure 13. Block diagram of a space-time coded, heterodyne-detection optical communication system. A binary sequence is first converted into a sequence of quadrature-amplitude modulation (QAM) symbols that are then space-time coded across *T* time slots and *N* transmit antennas. The space-time decoder operates over these same *T* time slots using *M* receive antennas.

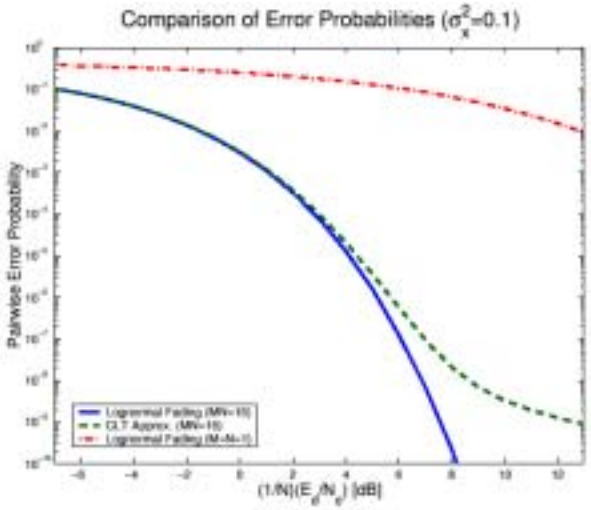

Figure 14. Comparison of pairwise error probabilities for the lognormal fading channel with moderate (σ_χ^2 = 0.1) fading and an orthogonal-design space-time code. Upper curve: single transmit antenna (*N* = 1), single receive antenna (*M* = 1). Middle curve: Central Limit Theorem approximation with multiple antennas (*MN* = 16). Bottom curve: exact result with multiple antennas (*MN* = 16).

We have also been studying the performance of direct-detection multiple aperture communications, shown in Fig. 15. As a prelude to treating the case of atmospheric fading channels, we have developed upper and lower bounds on the capacity of shot-noise limited multiple-input, multiple-output (MIMO) single-user communications operating under peak and average power constraints [19]. Our work, which build directly from previous work on the single-input, single-output (SISO) channel [20,21], provides exact capacity results in several interesting

limiting cases, e.g., low and high signal-to-background ratio, because the upper and lower bounds become coincident in these limits. Furthermore, see Fig. 16, the bounds can be quite close together even when operation is outside of the preceding special-case regimes. We are presently extending this work — which assumed arbitrary non-random path gains — to the case of lognormal fading.

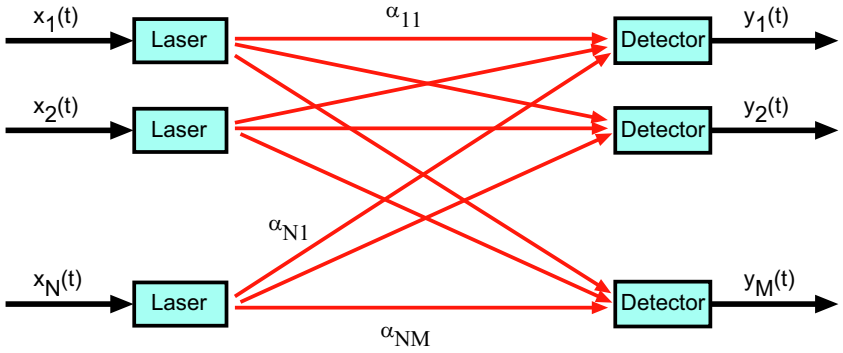

Figure 15. Block diagram of the multiple-input, multiple-output, single-user Poisson channel. A single-user information source modulates the power from *N* laser sources using waveforms $\{x_n(t)\}$. These lasers couple power to *M* shot-noise limited (Poisson statistics) photodetectors via the path gains $\{\alpha_{nm}\}$. The single-user receiver decodes the transmitted information from observations of the Poisson processes $\{y_m(t)\}$.

The preceding heterodyne-detection and direct-detection analyses apply to shot-noise limited performance regimes. In many realistic scenarios such sensitivity may be unattainable. To understand atmospheric optical communication performance outside the shot-noise-limited regime, we have begun a study of the performance of optically-amplified photodiode reception. We have evaluated the error probability of on-off-keyed (OOK) binary communication through turbulence when a single receive aperture is used, and we are in the process of extending the analysis to include diversity reception.

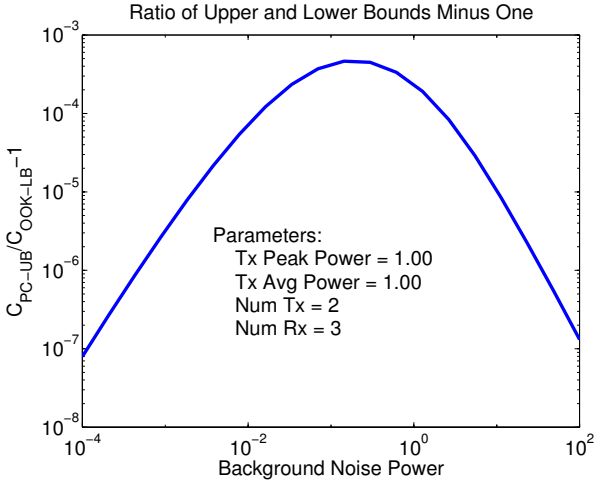

α_{nm}	$m=1$	$m=2$	$m=3$
$n=1$	0.2977	0.5760	0.1279
$n=2$	0.0692	0.6979	2.0322

Figure 16. Comparison of the upper and lower bounds on the capacity of the single-use MIMO Poisson channel for a particular set of path gains with *N* = 2 and *M* = 3.

In addition to the theoretical treatment of atmospheric optical communication, we are developing an experimental test bed to supplement and support the analytical work. We have completed the setup of an OC-48 (2.5-Gb/s) fiber-optic link in the laboratory, as shown schematically in Fig. 17. A cw laser at one of the ITU grid wavelengths (~1559 nm) is modulated with a bias-free OC-48 modulator before being launched into free space with a 10x telescope. After a short air path of 1.5 m, the light is collected with another 10x telescope and coupled into a single-mode optical fiber. The signal is then optically amplified with an erbium doped fiber amplifier (EDFA) to boost its signal strength, narrowband filtered to reduce the amplified spontaneous emission noise from the EDFA, and detected using a pin photodiode. The resultant electrical signal is amplified, low-pass filtered, and analyzed.

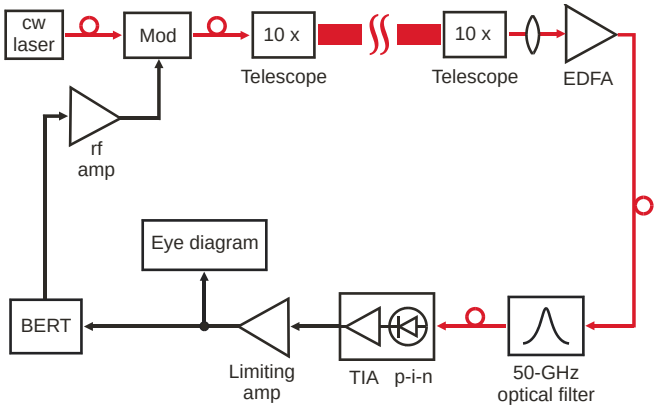

Figure 17. Schematic of 2.5-Gb/s fiber-optic link including a through-the-air portion between the two telescopes. Mod: OOK modulator; EDFA: erbium-doped fiber amplifier; TIA: transimpedance amplifier; BERT: bit error rate tester.

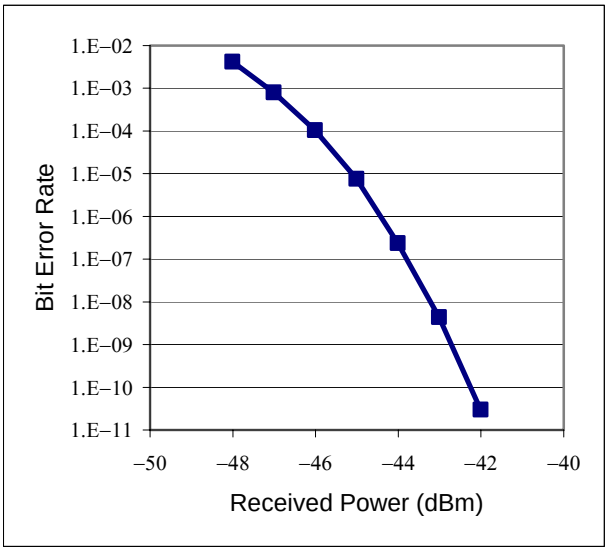

Figure 18. Bit error rate (BER) measurements vs. received optical power at the input of EDFA for laboratory OC-48 through-the-air link.

We have obtained preliminary baseline performance of the system to allow meaningful comparison when the short laboratory free-space path is replaced with an outdoor path and when multiple receivers are used. Figure 18 shows the bit error rate (BER) as a function of receiver power, as measured at the input to the EDFA. Initial measurements indicate a BER (10^{-9}) sensitivity of –43 dBm of receiver optical power. This is about 3 dB higher than expected and we

will examine our measurements and calculations to resolve the difference. We will soon implement diversity reception by adding receivers, and move the laboratory test bed to an outdoor site (for the free-space part) to evaluate communication performance under prevailing atmospheric conditions.

References

1. J. H. Shapiro, "Long-Distance High-Fidelity Teleportation using Singlet States," in *Quantum Communication, Measurement and Computing 3*, eds. O. Hirota and P. Tombesi (Kluwer, New York, 2001).

2. C. H. Bennett, G. Brassard, C. Crépeau, R. Jozsa, A. Peres, and W. K. Wootters, "Teleporting an Unknown Quantum State via Dual Classical and Einstein-Podolsky-Rosen Channels," *Phys. Rev. Lett*. 70, 1895-1899 (1993).

3. S. Lloyd, M. S. Shahriar, J. H. Shapiro, and P. R. Hemmer, "Long-Distance Unconditional Teleportation of Atomic States via Complete Bell State Measurements," *Phys. Rev. Lett*. 87, 167903 (2001).

4. J. H. Shapiro and N. C. Wong, "An Ultrabright Narrowband Source of Polarization-Entangled Photon Pairs," *J. Opt. B: Quantum Semiclass*. Opt. 2, L1-L4 (2000).

5. J. H. Shapiro, "Architectures for Long-Distance Quantum Teleportation," *New J. Phys*., forthcoming.

6. C. E. Kuklewicz, E. Keskiner, F. N. C. Wong, and J. H. Shapiro, "A High-Flux Entanglement Source Based on a Doubly-Resonant Optical Parametric Amplifier," *J. Opt. B: Quantum Semiclass. Opt*., forthcoming.

7. D. M. Greenberger, M. A. Horne, and A. Zeilinger, "Going Beyond Bell's Theorem," in *Bell's Theorem, Quantum Theory, and Conceptions of the Universe*, ed. M. Kafatos (Dordrecht, Kluwer, 1989).

8. M. Hillery, V. Buzek, and A. Berthiaume, "Quantum Secret Sharing," *Phys. Rev. A* 59,1829-1834 (1999).

9. D. Bouwmeester, J.-W. Pan, M. Daniell, H. Weinfurter, and A. Zeilinger, "Observation of Three-Photon Greenberger-Horne-Zeilinger Entanglement," *Phys. Rev. Lett*. 82, 1345-1349 (1999).

10. C. Santori, M. Pelton, G. Solomon, Y. Dale, and Y. Yamamoto, "Triggered Single Photons from a Quantum Dot," *Phys. Rev. Lett*. 86,1502-1505 (2000).

11. V. Giovannetti, S. Lloyd, and L. Maccone, "Quantum-Enhanced Positioning and Clock Synchronization," *Nature* 412, 417-419 (2001).

12. V. Giovannetti, L. Maccone, J. H. Shapiro, and F. N. C. Wong, "Generating Entangled Two-Photon States with Coincident Frequencies," submitted to *Phys. Rev. Lett*.

13. V. Giovannetti, S. Lloyd, and L. Maccone, "Time-Independent Clock Synchronization," submitted to *Nature*.

14. A. Steinberg, P. G. Kwiat, and R. Y. Chiao, "Dispersion Cancellation in a Measurement of the Single-Photon Propagation Velocity," *Phys. Rev. Lett*. 68, 2421-2425 (1992).

15. V. Giovannetti, S. Lloyd, L. Maccone, and F. N. C. Wong, “Clock Synchronization with Dispersion Cancellation,” *Phys. Rev. Lett*. 87,117902 (2001).

16. V. Tarokh, N. Seshardri, and A. Calderbank, “Space-Time Codes for High Data Rate wireless Communication: Performance Criteria and Code Construction,” *IEEE Trans. on Inform. Theory* IT-44, 744-765 (1998).

17. J. H. Shapiro, “Imaging and Optical Communication through Atmospheric Turbulence,” in *Laser Beam Propagation in the Atmosphere*, ed. J. W. Strohbehn (Springer, Berlin, 1978).

18. S. M. Haas, J. H. Shapiro, and V. Tarokh, “Space-Time Codes for Wireless Optical Communications,” *EURASIP J. App. Signal Proc*., forthcoming.

19. S. M. Haas, “Capacity of the Multiple-Input, Multiple-Output Poisson Channel,” paper presented at the Workshop on Stochastic Theory and Control, Lawrence, KS, October 18-20, 2001.

20. M. A. Davis, “Capacity and Cutoff Rate for Poisson-Type Channels,” *IEEE Trans. on Inform. Theory*, IT-26, 710-715 (1980).

21. A. D. Wyner, “Capacity and Error Exponent for the Direct Detection Photon Channel—Part I,” *IEEE Trans. on Inform. Theory*, IT 34, 1449-1461 (1988).

Publications

Journal Articles, Published

S. Lloyd, M. S. Shahriar, J. H. Shapiro, and P. R. Hemmer, “Long-Distance Unconditional Teleportation of Atomic States via Complete Bell State Measurements,” *Phys. Rev. Lett*. 87, 167903 (2001).

V. Giovannetti, S. Lloyd, L. Maccone, and F. N. C. Wong, “Clock Synchronization with Dispersion Cancellation,” *Phys. Rev. Lett*. 87,117902 (2001).

S. Lloyd, J. H. Shapiro, and F. N. C. Wong, “Quantum Magic Bullets by Means of Entanglement,” J. Opt. Soc. Am. B 19, 312-318 (2002).

Journal Articles, Accepted for Publication

C. E. Kuklewicz, E. Keskiner, F. N. C. Wong, and J. H. Shapiro, “A High-Flux Entanglement Source Based on a Doubly-Resonant Optical Parametric Amplifier,” *J. Opt. B: Quantum Semiclass. Opt*., forthcoming.

A. Lvovsky and J. H. Shapiro, “Nonclassical Character of Statistical Mixtures of the Single-Photon and Vacuum Optical States,” *Phys. Rev. A*, forthcoming.

J. H. Shapiro, “Architectures for Long-Distance Quantum Teleportation,” *New J. Phys*., forthcoming.

S. M. Haas, J. H. Shapiro, and V. Tarokh, “Space-Time Codes for Wireless Optical Communications,” *EURASIP J. App. Signal Proc*., forthcoming.

Journal Articles, Submitted for Publication

V. Giovannetti, L. Maccone, J. H. Shapiro, and F. N. C. Wong, "Generating Entangled Two-Photon States with Coincident Frequencies," submitted to *Phys. Rev. Lett*.

Book/Chapters in Books

J. H. Shapiro, "Long-Distance High-Fidelity Teleportation using Singlet States," in *Quantum Communication, Measurement and Computing 3*, eds. O. Hirota and P. Tombesi (Kluwer, New York, 2001).

Meeting Papers, Presented

J. H. Shapiro, "Architectures for Long-Distance Quantum Communication," paper presented at the Workshop on Quantum Interference and Cryptographic Keys, Cargèse, Corsica, April 8-13, 2001.

J. H. Shapiro, "Architectures for Long-Distance Quantum Communication," paper presented at the NSA/NRO Workshop on Quantum Cryptographic Applications, McLean, VA, July 30-31, 2001.

S. M. Haas., "Capacity of the Multiple-Input, Multiple-Output Poisson Channel," paper presented at the Workshop on Stochastic Theory and Control, Lawrence, KS, October 18-20, 2001.

Meeting Papers, Published

S. Lloyd, J. H. Shapiro, and N. C. Wong, "Quantum Magic Bullets via Entanglement," *Digest of Quantum Electronics and Laser Science Conference*, Baltimore, MD, May 6-11, 2001.

C. E. Kuklewicz, E. Keskiner, F. N. C. Wong, and J. H. Shapiro, "A High-Flux Entanglement Source Based on a Doubly-Resonant Optical Parametric Amplifier," *Proceedings of the Seventh International Conference on Squeezed States and Uncertainty Relations*, Boston, MA, June 4-8, 2001.

J. H. Shapiro, "Architectures for Long-Distance Quantum Communication," *Proceedings of the Seventh International Conference on Squeezed States and Uncertainty Relations*, Boston, MA, June 4-8, 2001.

S. M. Haas, J. H. Shapiro, and V. Tarokh, "Space-Time Codes for Wireless Optical Channels," *Digest of the International Symposium on Information Theory*, Washington, DC, June 24-29, 2001.

Theses

Emily W. Nelson, *Counting Statistics of a System to Produce Entangled Photon Pairs*, S.M. thesis, Department of Electrical Engineering and Computer Science, MIT, 2001.

Eser Keskiner, *An Ultra-Bright Narrowband Source of Polarization-Entangled Photons*, M.Eng. thesis, Department of Electrical Engineering and Computer Science, MIT, 2001.